Supplementary Information (SI) for Materials Horizons.

Supplementary Information

Flexible Films Assembled from Polyimide Microparticles Loaded with Ionic Liquids for Iontronic Sensors

Minhan Cheng, Qianyang Li, Kefan Chen, Ming Wen, Mao Zhang, Hua Deng*

College of Polymer Science and Engineering, State Key laboratory of Advanced Polymer Materials, Sichuan University, Chengdu 610065, China

*Corresponding author: huadeng@scu.edu.cn

This file includes:

Supplementary Note S1 to S2
Supplementary Figure S1 to S29
Supplementary Table S1 to S3

Supplementary Note S1

Theoretical evaluation of the flow regime of nonsolvent phase ionic liquid

To determine the flow regime of the nonsolvent phase, the Reynolds number (*Re*) is a viable evaluation strategy:

$$Re = \frac{\rho v d}{\mu} \#(S1)$$

where ρ and μ represent the density and dynamic viscosity of the precipitation medium, respectively. Notably, μ should represent the viscosity under specific flow conditions (e.g., temperature and shear rate), rather than the zero-shear viscosity. Since the outer cylinder remains stationary, the characteristic length d is defined as the gap between the stator and the rotor (~1.3 mm), while the fluid velocity v is determined by the radius and angular velocity of the rotor. However, owing to the serrations on the stator-rotor and the probability of cavitation at high shear rates, it is challenging to precisely estimate the exact shear rates and flow characteristics. Furthermore, the heat generated by sustained high-speed friction causes local temperature to rise rapidly; consequently, the dynamic viscosity can only be roughly estimated.[1,2] Here, v is estimated at 20 m/s, with a local temperature of 50 °C at a rotor speed of 20,000 rpm. According to report,[3] the density of [EMIm][NTf$_2$] at 50 °C is 1.493 g/cm^3 and its viscosity is 15.57 mPa·s. Also, under our processing conditions, the IL is treated as a Newtonian fluid (viscosity independent of shear rate). Therefore, the calculated *Re* is approximately 2500, indicating that the IL is in a transitional flow state.

Supplementary Note S2

Theoretical calculation of strain-load relationship in four-point bending model

For the four-point bending model constructed in micro-strain detection, based on classical mechanics theory,[4] the tensile strain distribution on the lower surface of quartz glass substrate follows the following formula:

$$\varepsilon = \frac{\sigma}{E} \# (S2)$$

where ε and σ denote the bending strain and stress, respectively. σ can be expressed as follows:

$$\sigma = \frac{My}{I} \# (S3)$$

where M is the bending moment, y represents the vertical distance from the neutral axis, and I denotes the moment of inertia of cross-section. M and I can be calculated using the following equations:

$$M = \frac{1}{2} Fa \# (S4)$$

$$I = \frac{1}{12} bh^3 \# (S5)$$

where F represents the total force applied by the upper clamp, and a, b, and h respectively correspond to the lever arm, the width and the thickness of the substrate. Then, the lateral strain at the center of the bottom ε_{xx} can be equivalently expressed as:

$$\varepsilon_{xx} = \frac{6Fay}{Ebh^3} \# (S6)$$

Based on the E (~60 GPa) and geometric parameters of quartz glass, the relationship between ε_{xx} and the total load F can be expressed as follows:

$$\varepsilon_{xx} = 4.6875 \times 10^{-6} F \# (S7)$$

When $F = 2$ N and 4.5 N, the calculated values of ε_{xx} are 9.375 ppm and 21.094 ppm, respectively. Correspondingly, the linear fit to the simulation results in FEA yields the relationship between ε_{xx} and F as: $\varepsilon_{xx} = 4.6325 \times 10^{-6} F$, which indicates that the simulation results closely match the theoretical calculations and are consistent with the classical mechanics model.

Supplementary Figures and Tables

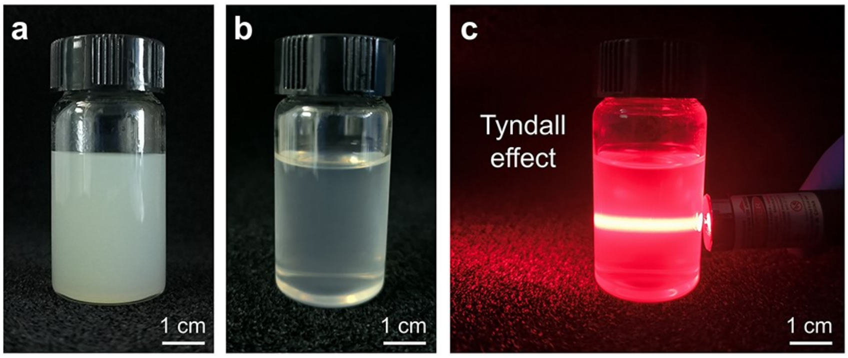

Figure S1. (a) Optical photograph of the precipitated PAA microparticles dispersed in the IL suspension (3 wt%), (b) diluted suspension, and (c) the Tyndall effect generated under laser irradiation.

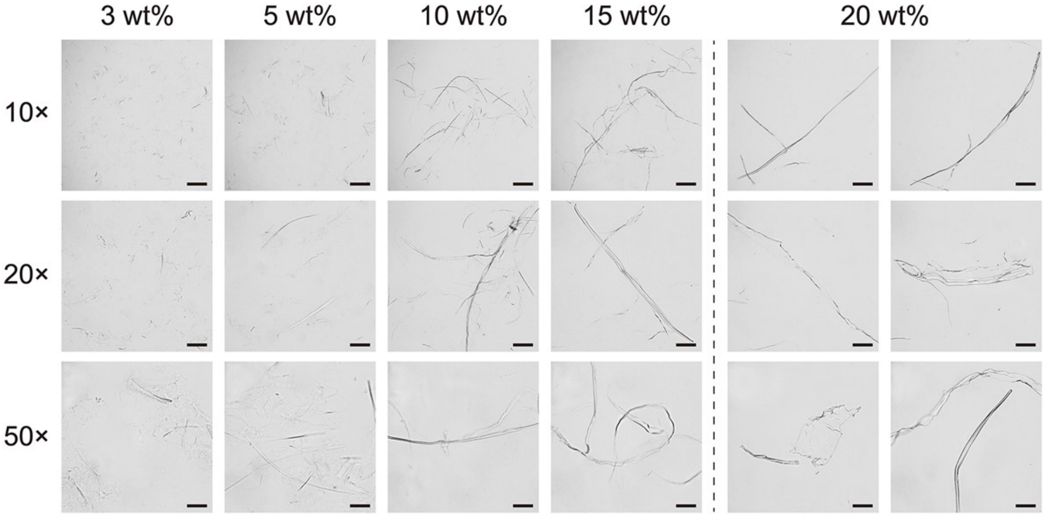

Figure S2. Optical microscope images of microparticles precipitated by shear in IL from PAA/DMAc solutions of varying concentrations. As solution concentration increases, microparticle size grows while morphology diversifies. The left panel indicates objective magnification: 10×, 20×, and 50× correspond to scale bars of 100 μm, 50 μm, and 20 μm, respectively.

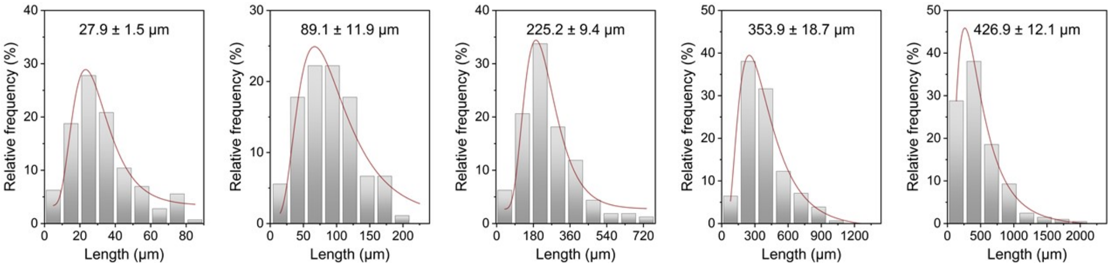

Figure S3. Length distribution of fibrous microparticles formed by precipitating from PAA solutions of varying initial concentrations (increase from 3 wt% to 20 wt% from left to right).

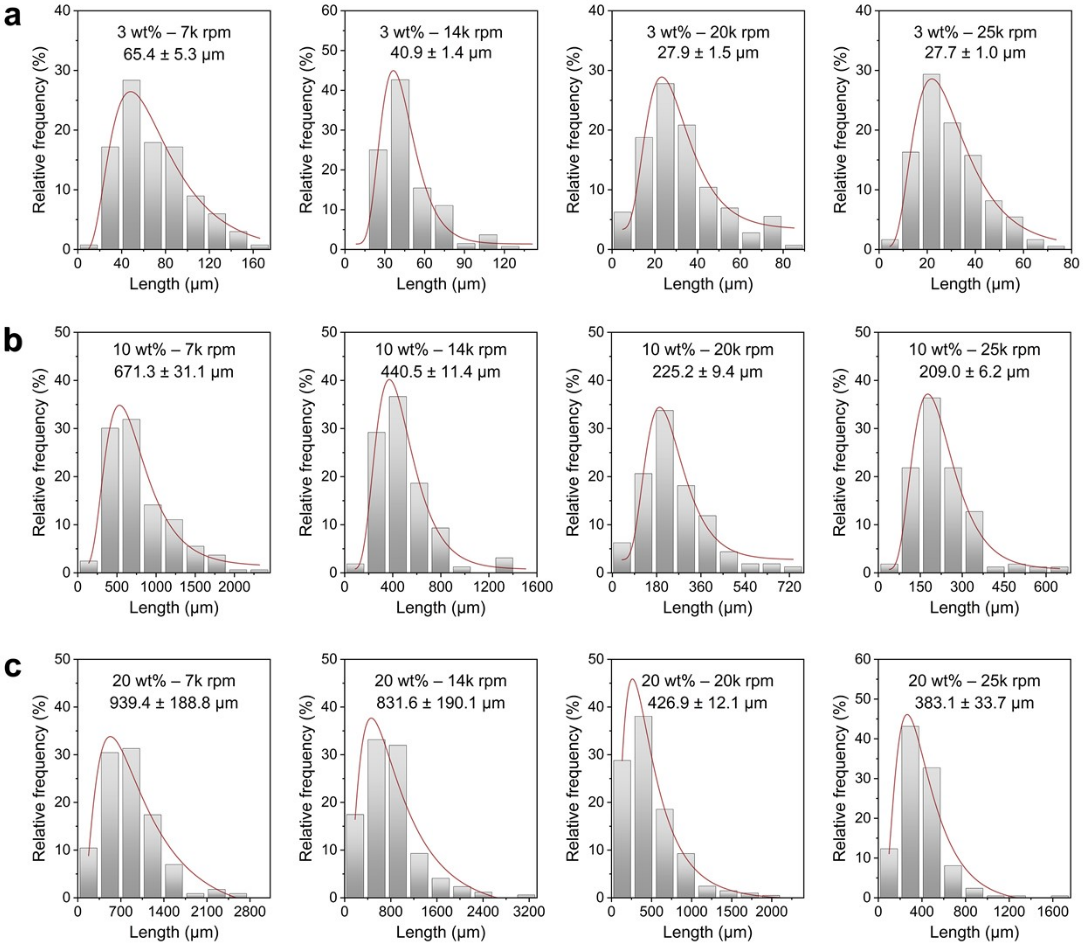

Figure S4. Length distributions of fibrous microparticles formed by precipitation from PAA solutions of (a) 3 wt%, (b) 10 wt%, and (c) 20 wt% under various rotor speeds (7,000, 14,000, 20,000, and 25,000 rpm).

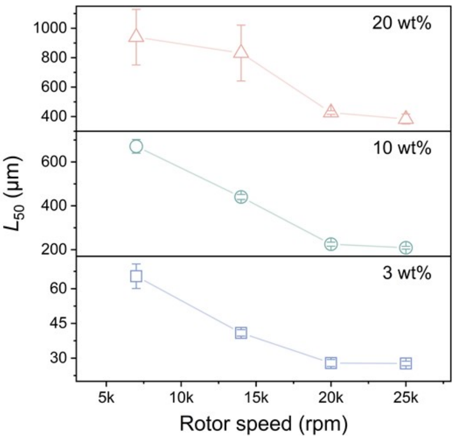

Figure S5. The median microparticle length (L_{50}) as a function of rotor speed for three different concentrations. As the rotor speed increases, both the L_{50} and distribution width gradually decrease, with a more pronounced reduction occurring below 20,000 rpm.

Figure S6. Optical images of free-standing PAA/DMAc/IL film and PI/IL film (PIF) during fabrication process (scale bars: 1 cm).

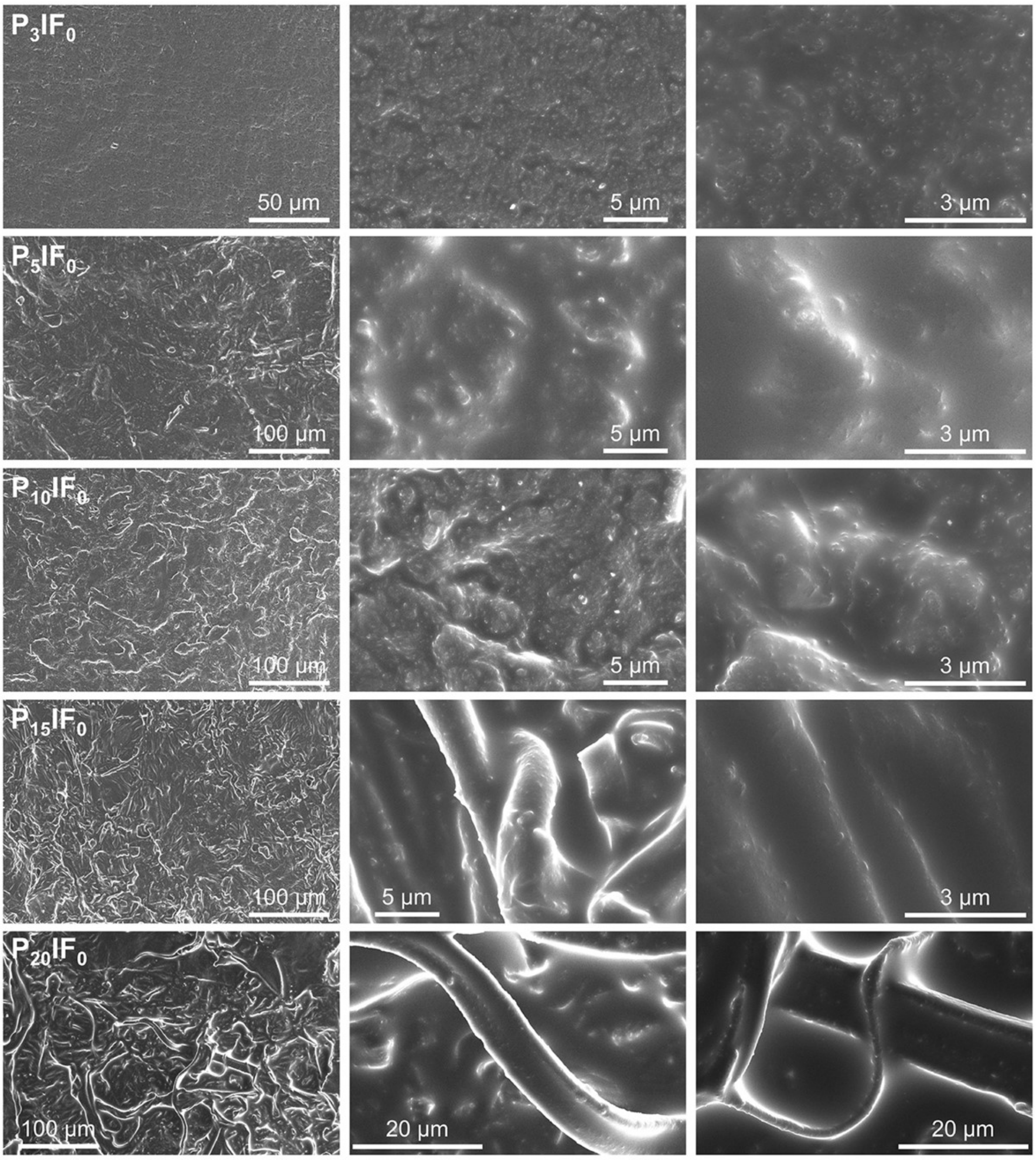

Figure S7. SEM images at different magnification levels showing the surface morphology of PIFs prepared from PAA solutions with various initial concentrations. All film surfaces are coated with IL layer. The surface of films formed by small-sized particles exhibits relative flat. As the initial solution concentration increases, particle size grows and surface roughness intensifies. When the concentration reaches 15 wt%, large-sized particles with high aspect ratios, wrapped in IL, can be observed intertwining with one another.

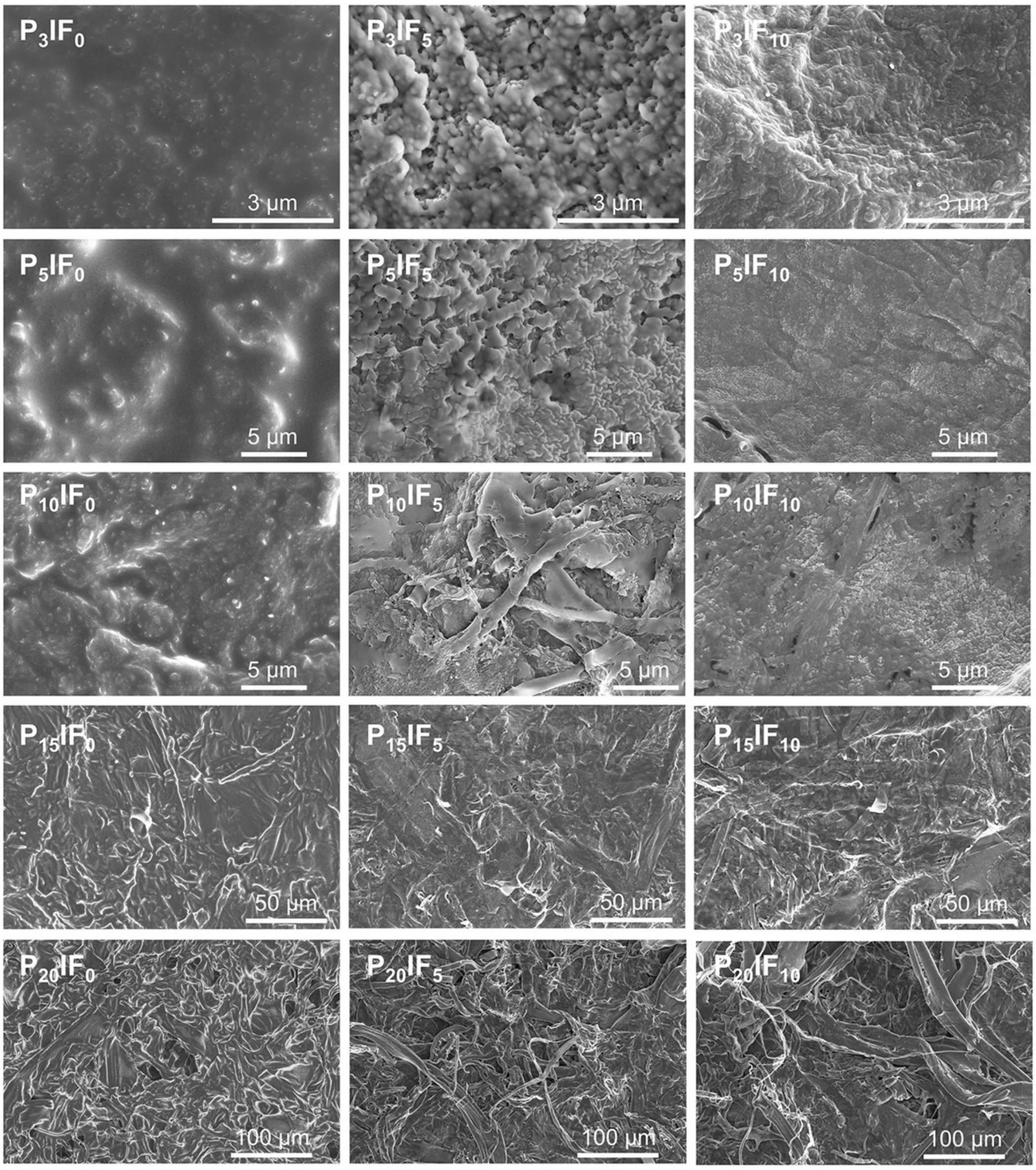

Figure S8. SEM images of the surface morphology of PIFs prepared from PAA solutions with various initial concentrations and subjected to different cold-pressing pressures. As cold-pressing pressure increases, free IL within films is removed, gradually revealing the surface morphology outline. After cold-pressing at 5 MPa, the particle aggregate network basically retains its structure due to PI's inherent high modulus, with abundant pores visible within. However, high pressure at 10 MPa causes the smaller, more uniformly shaped particle aggregate network to collapse and densify. Only the larger, irregularly shaped particles with high aspect ratio fail to pack tightly, remaining in a randomly entangled distribution state.

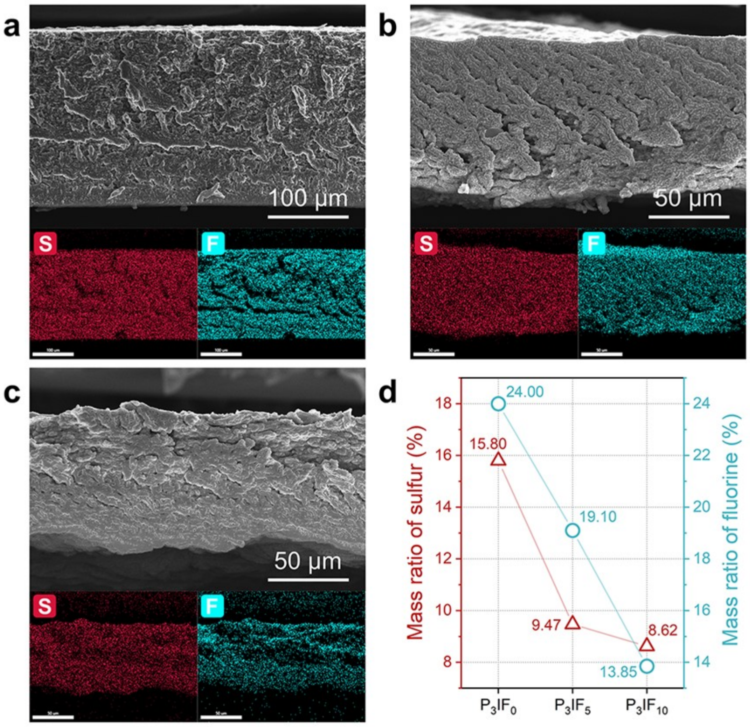

Figure S9. SEM images of cross-sections of P_3IFs after different cold-pressing pressures and corresponding sulfur (S) and fluorine (F) element distributions: (a) P_3IF_0 (thickness ~ 215 μm), (b) P_3IF_5 (thickness ~ 100 μm), and (c) P_3IF_{10} (thickness ~ 85 μm). (d) The mass ratio of S and F in the cross-section of P_3IFs gradually decreases with increasing cold-pressing pressure. Since only anion ($[NTf_2]^-$) in PIFs contains S and F, which indicates that the cold-pressing process densifies the network (reducing film thickness) and removes some of the unbound IL.

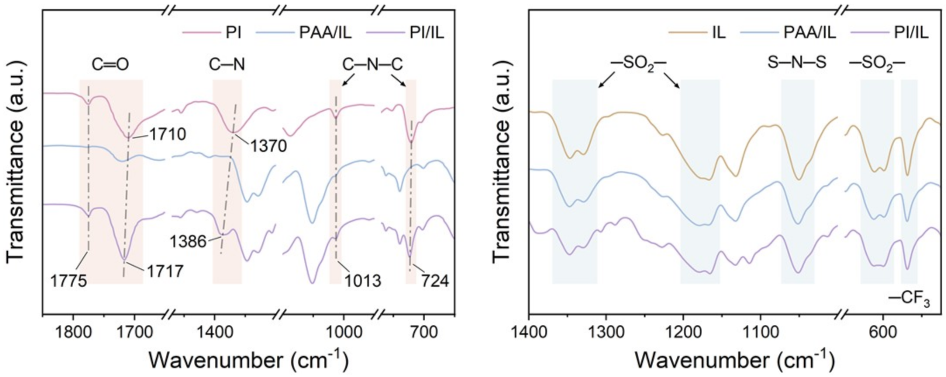

Figure S10. FT-IR comparison magnified spectra of IL ([EMIm][NTf$_2$]), neat PI, PAA/IL film, and PI/IL film. The left compares the positions of characteristic peaks for PI across different films, while the right shows the positions of characteristic peaks for IL. Compared to neat PI, the stretching vibration peaks of the C═O bond and C─N bond in the PIF spectrum (at 1717 cm^{-1} and 1386 cm^{-1}) occur at higher wavenumbers.

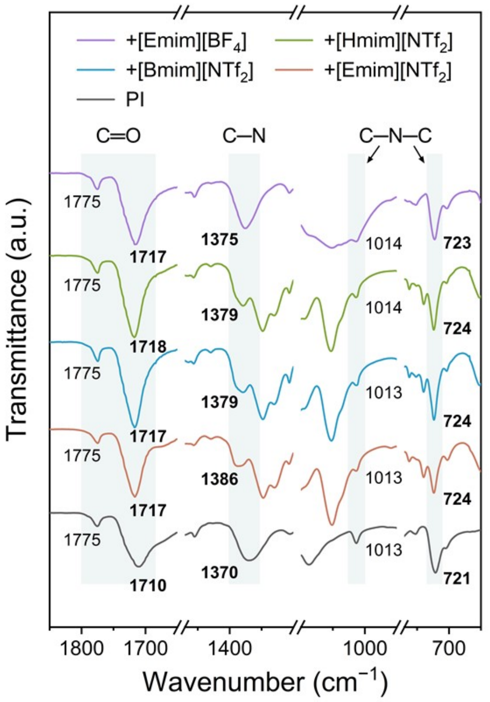

Figure S11. Comparison of FT-IR spectra for PI and composite films with different kinds of ILs. The characteristic peaks of PI at 1710 cm^{-1}, 1370 cm^{-1}, and 721 cm^{-1} exhibit varying degrees of blue shift after composite formation with various ILs (marked in bold).

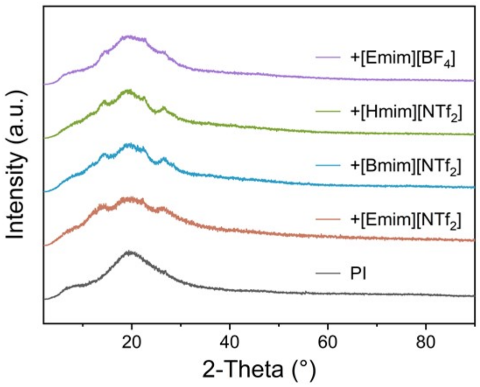

Figure S12. Comparison of X-ray diffraction patterns for PI and composite films with different types of ILs.

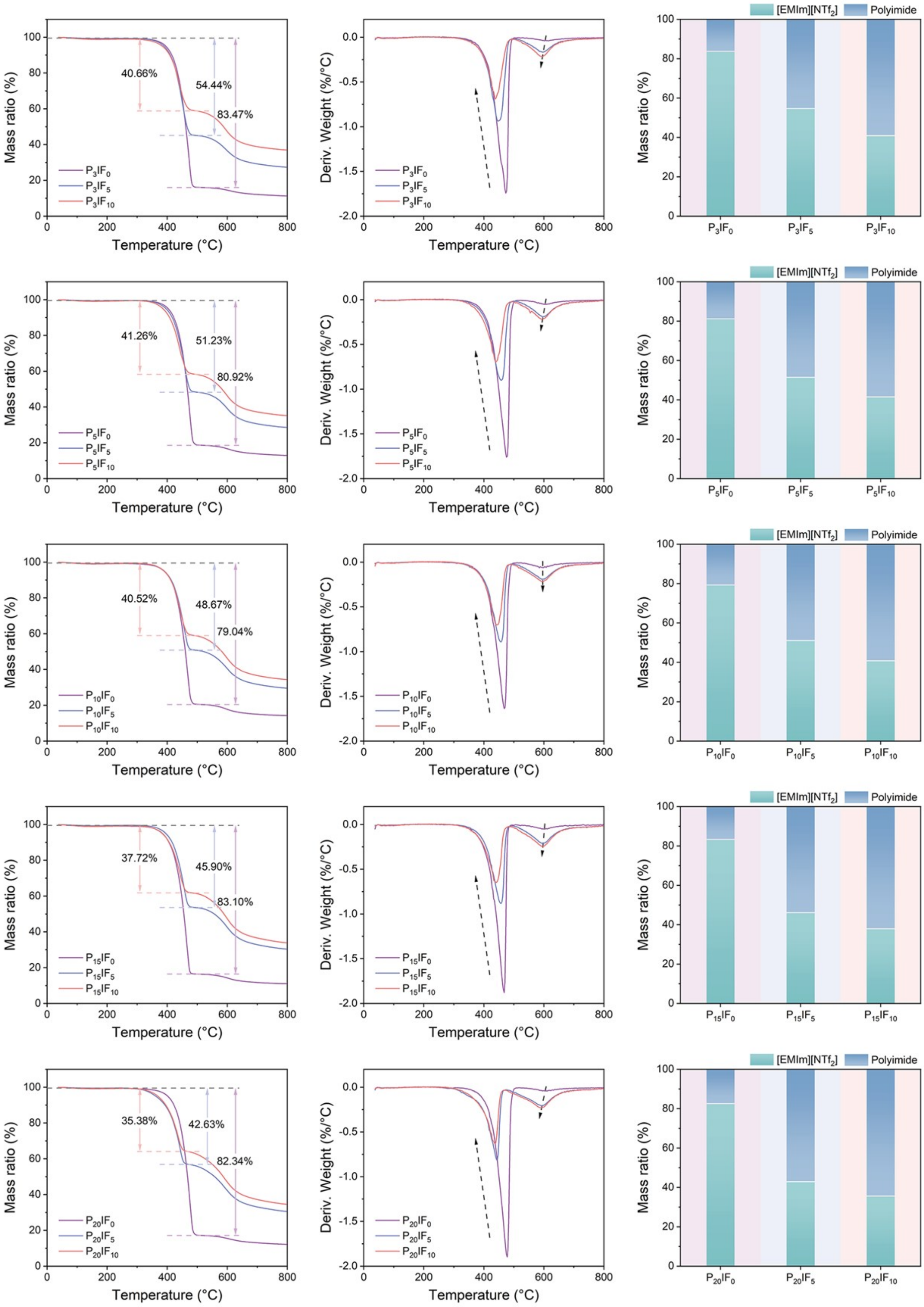

Figure S13. TG and DTG curves of various PIFs and the mass ratio of PI to IL in films. For PIFs composed of microparticles with different morphologies, the initial mass ratio of IL to PI can reach approximately 4:1. Upon application of normal pressure, IL leaks out from within the network, and its mass fraction within PIFs decreases as the cold-pressing pressure increases. Meanwhile, the temperature at which

IL and PI in PIFs achieve maximum decomposition rates shows a slight downward trend.

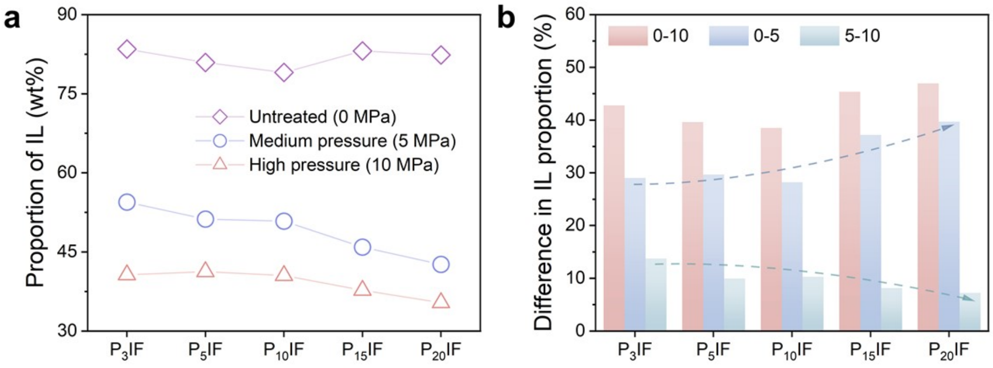

Figure S14. (a) Comparison of the mass proportion of IL in PIFs processed with PAA solutions of various initial concentrations and subjected to different cold-pressing pressures. (b) Comparison of IL content differences in PIFs after different cold-pressing pressure treatments (numbers in the legend indicate pressure values). At 5 MPa pressure, more IL leaks out from within the network formed by larger microparticles. As the pressure further increases to 10 MPa, the network composed of smaller microparticles collapses and densifies, thereby draining out more IL.

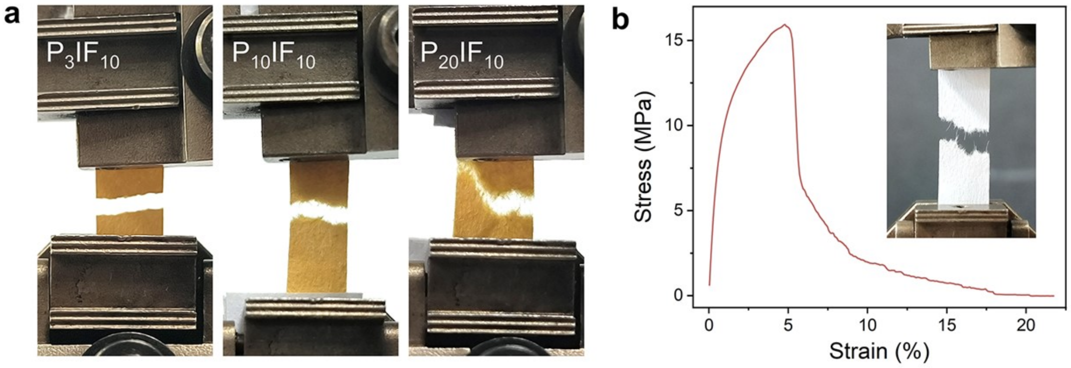

Figure S15. (a) Optical images of several PIFs at fracture during constant strain rate tensile testing on a dynamic mechanical analyzer. As particle size and aspect ratio increase, the fracture edge of the film gradually exhibits a "fuzzy" fibrous fracture morphology. (b) Stress-strain curve of plant fiber-based office paper under identical tensile conditions. The inset shows an optical photograph of the fracture point, clearly revealing fiber pull-out at the fracture.

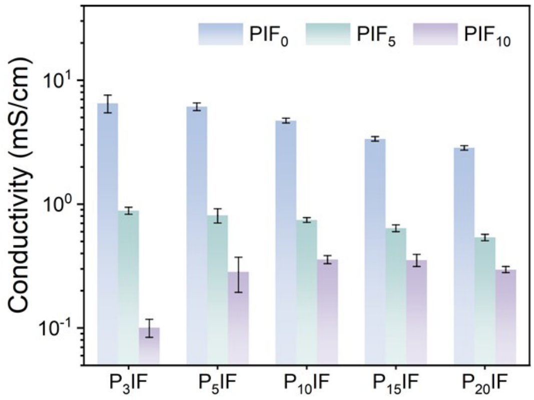

Figure S16. Comparison of the electrical conductivity of various PIFs. The conductivity of PIF decreases with increasing cold-pressing pressure and decreasing internal IL content.

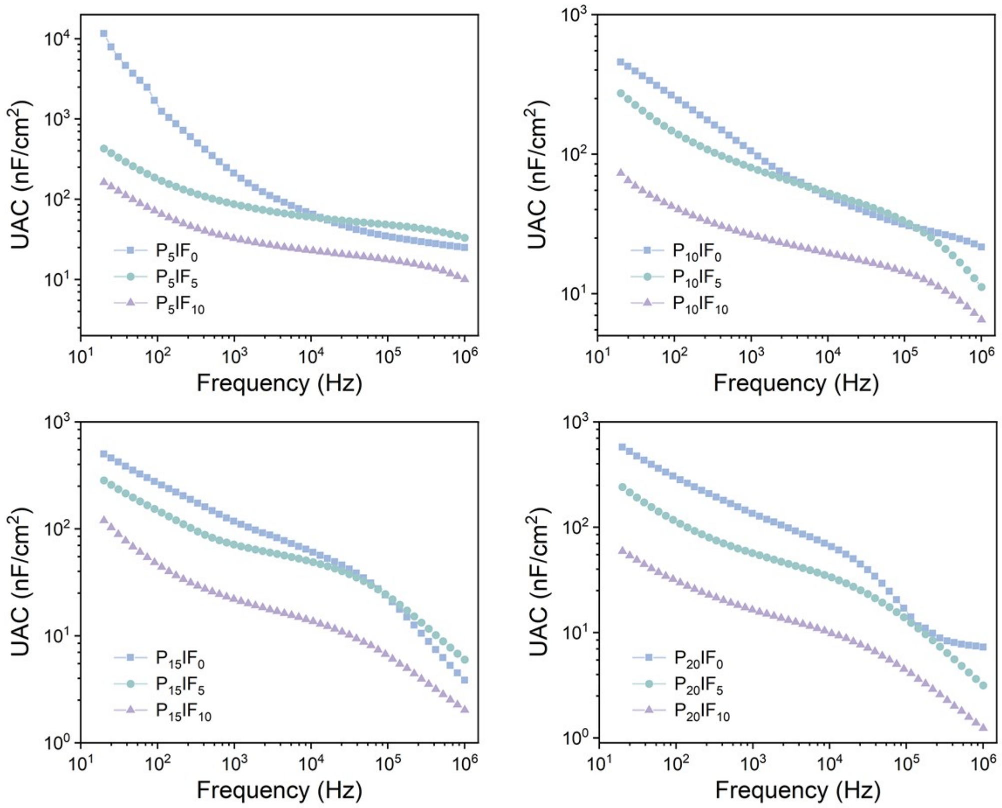

Figure S17. Comparison of unit-area capacitance as a function of frequency for various PIFs (20–1M Hz).

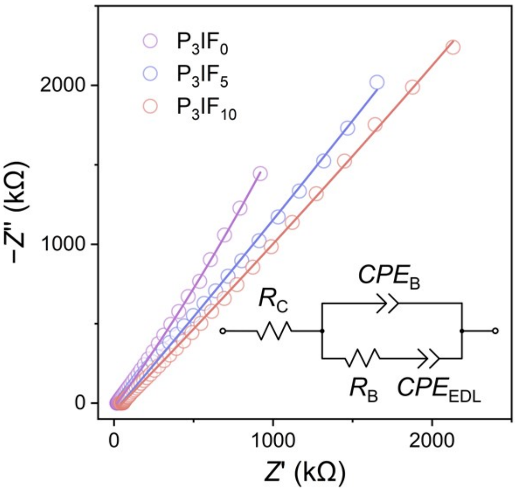

Figure S18. Nyquist plots of P_3IFs subjected to different pressure treatments. The inset shows the circuit model used for fitting the data. R_C represents the contact resistance, R_B represents the bulk resistance, CPE_B represents the constant phase element of the bulk, and CPE_{EDL} represents the constant phase element of the EDL.

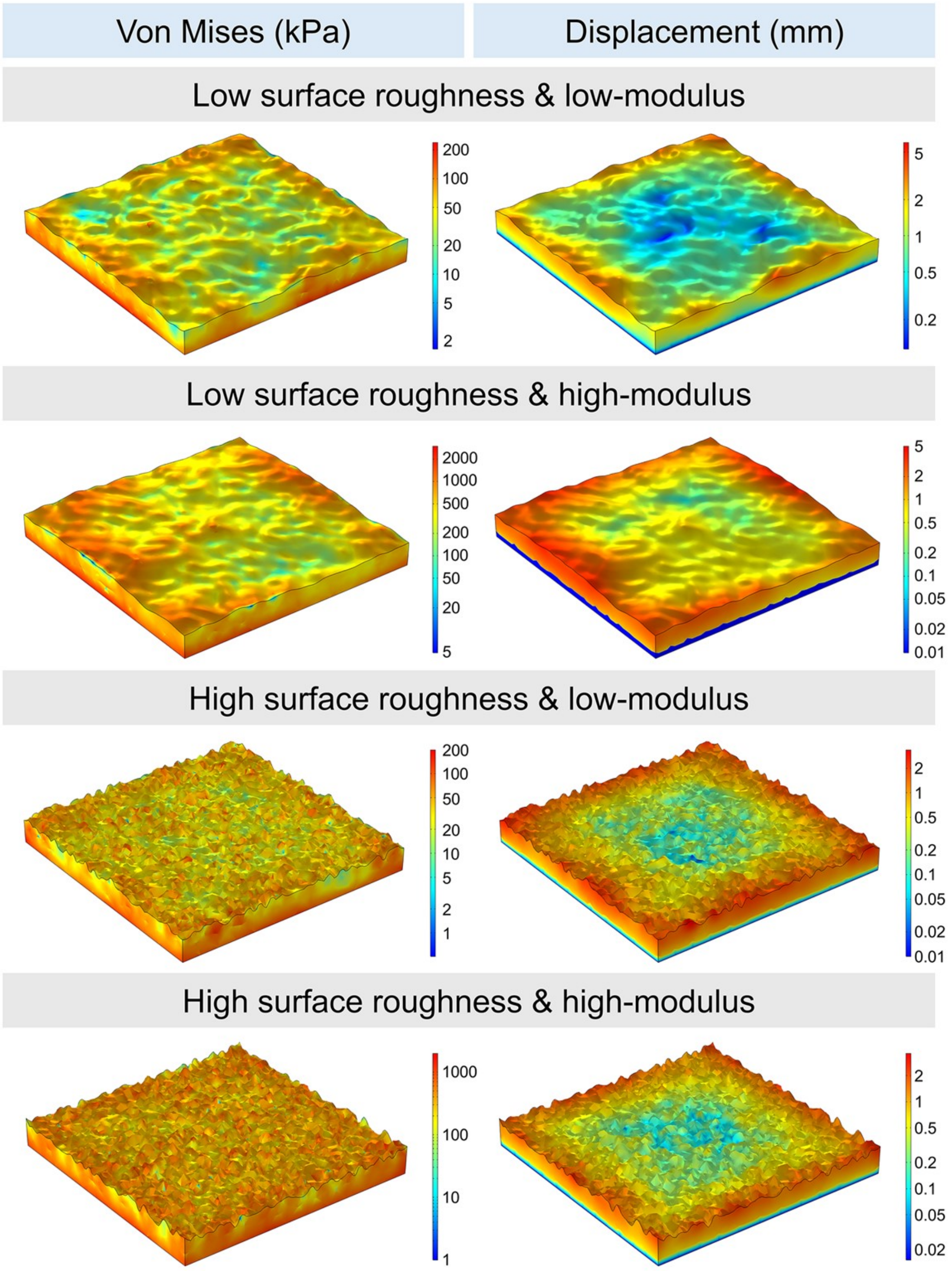

Figure S19. 3D-FEA of stress distribution and displacement distribution when sensing structures with different moduli and surface roughnesses reach contact saturation under pressure loading.

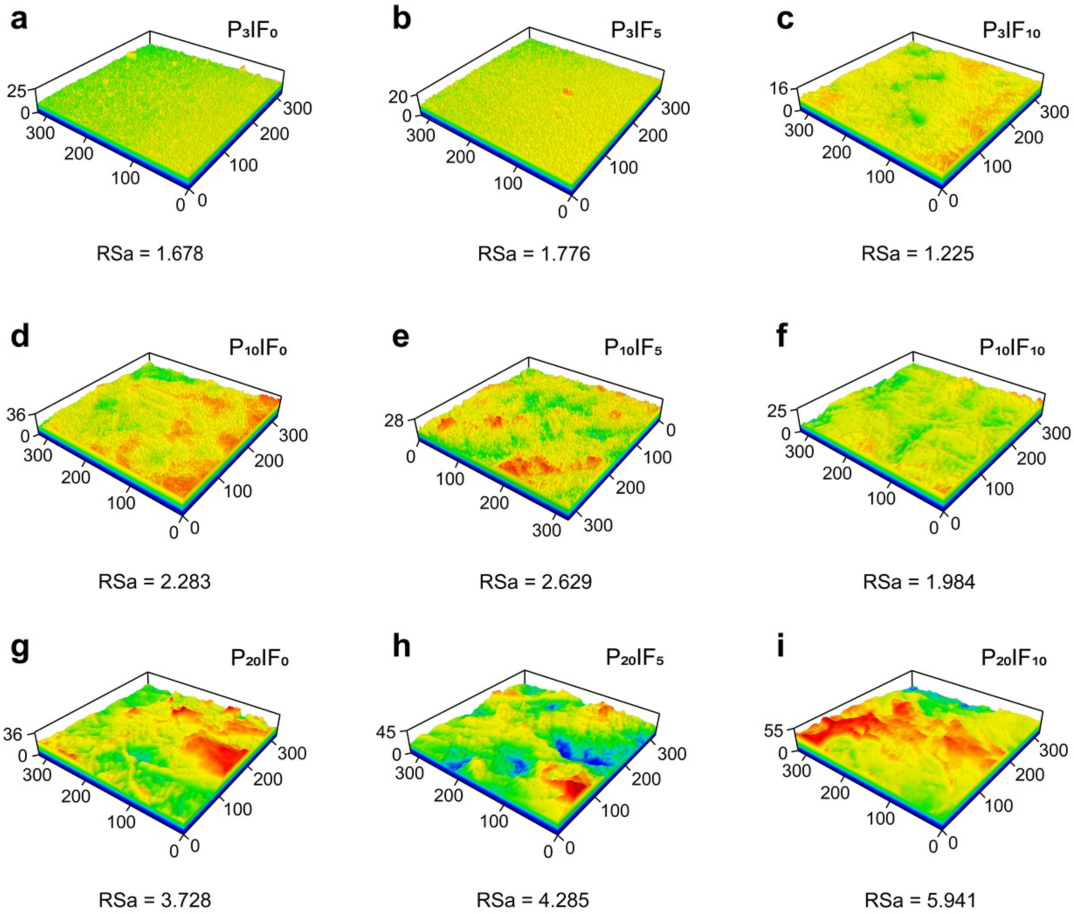

Figure S20. Comparison of 3D surface topography images and areal arithmetic mean height (RSa) of (a–c) P_3IFs, (d–f) P_{10}IFs, and (g–i) P_{20}IFs obtained by confocal laser scanning microscope.

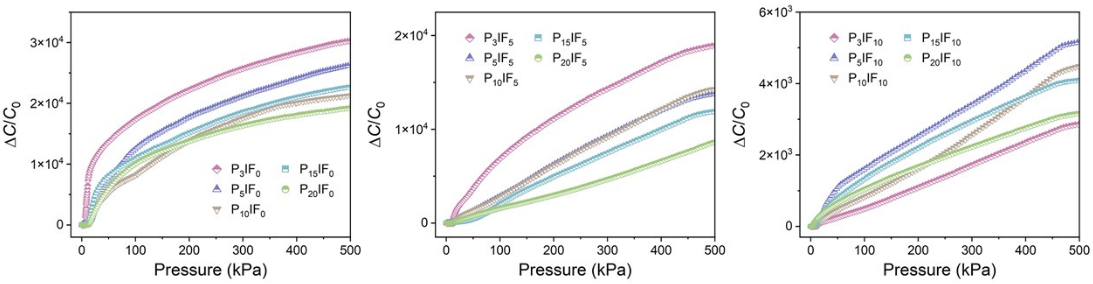

Figure S21. Response curves of relative capacitance changes ($\Delta C/C_0$) in PIFS constructed from different PIFs to pressure. The overall response sensitivity decreases as pressure increases, while linearity exhibits the opposite trend.

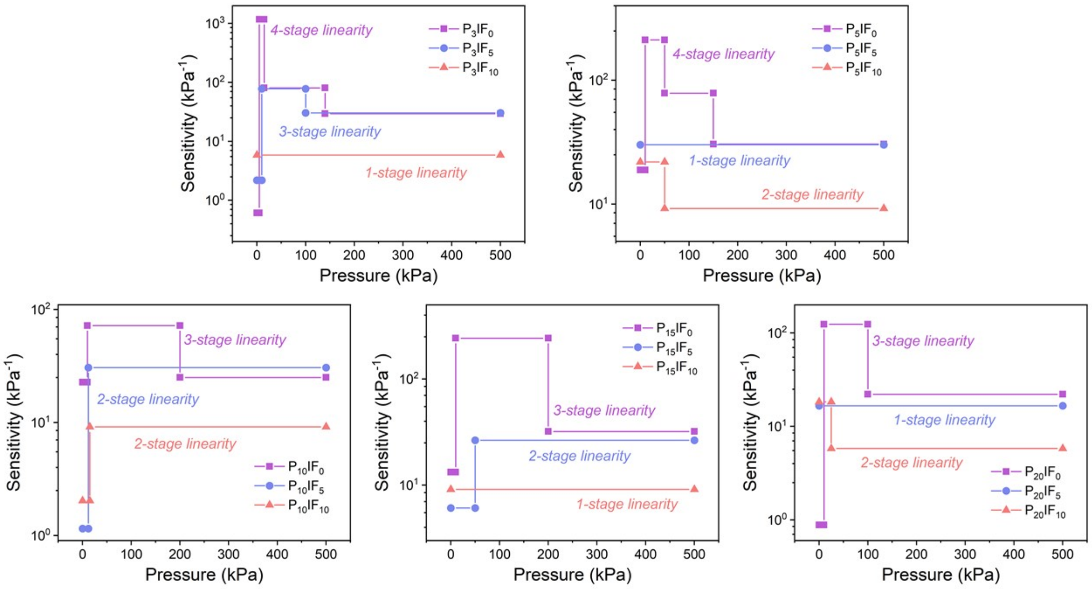

Figure S22. Comparison of fitting sensitivity results for PIFS constructed based on different PIFs. The sensitivity and number of linear response stages of sensors decrease as cold-pressing pressure increases.

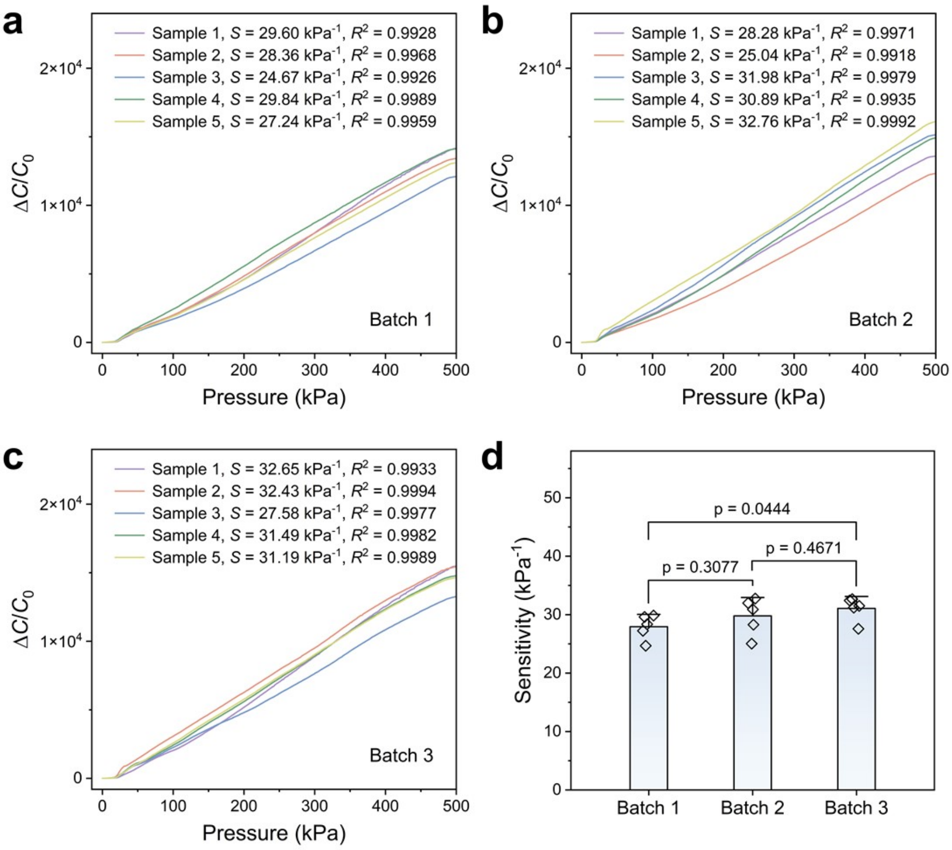

Figure S23. (a–c) Comparison of the electromechanical performance of pressure sensors based on P_5IF_5 from three independent batches (5 sensors per batch, 15 sensors in total). (d) Analysis of statistical significance in sensitivity among the three batches of iontronic devices. The $\Delta C/C_0$ versus pressure curves for the five samples within each batch cluster closely, with individual sensitivities range from 24.67 to 32.76 kPa^{-1} and all $R^2 > 0.99$, indicating excellent sample-to-sample consistency within each batch. Batch-to-batch comparison reveals mean sensitivities of 27.94 ± 1.88 kPa^{-1} (Batch 1), 29.79 ± 2.82 kPa^{-1} (Batch 2), and 31.07 ± 1.83 kPa^{-1} (Batch 3). Statistical analysis shows no significant difference between Batch 1 and Batch 2 or between Batch 2 and Batch 3, while the difference between Batch 1 and Batch 3 is statistically significant but modest, corresponding to a ~11% variation in mean sensitivity.

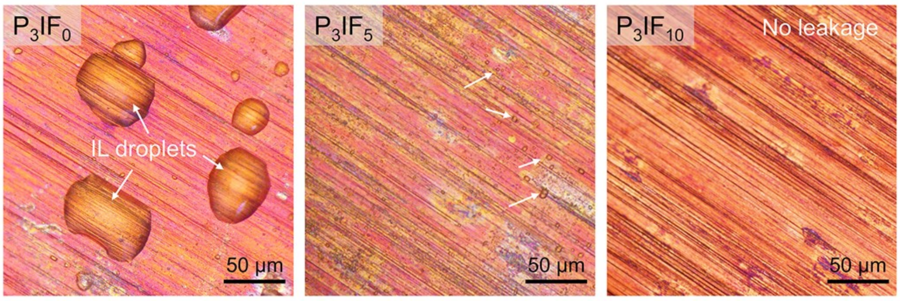

Figure S24. Comparison of micrographs of the top electrodes obtained after disassembly of iontronic sensors constructed based on P_3IF_0, P_3IF_5, and P_3IF_{10} following 5 min of static pressure at 100 kPa. The untreated film leaked liquid after compression, leaving large droplets of IL on the top electrode (indicated by white arrows). In contrast, after medium-to-high pressure cold-pressing, virtually no IL seeped onto the electrode surface.

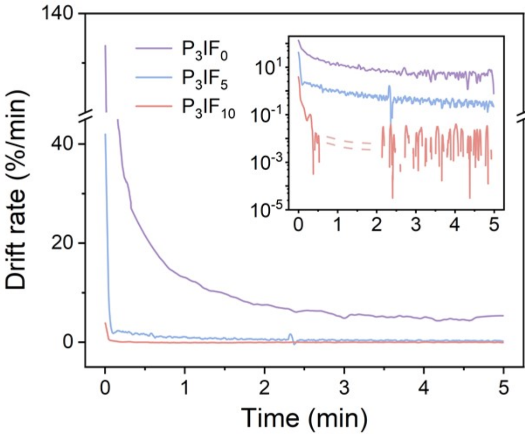

Figure S25. Capacitive response signal drift rates of three iontronic pressure sensors over time within 5 min. The inset shows a logarithmic vertical axis version, with the double dashed line section indicating negative values.

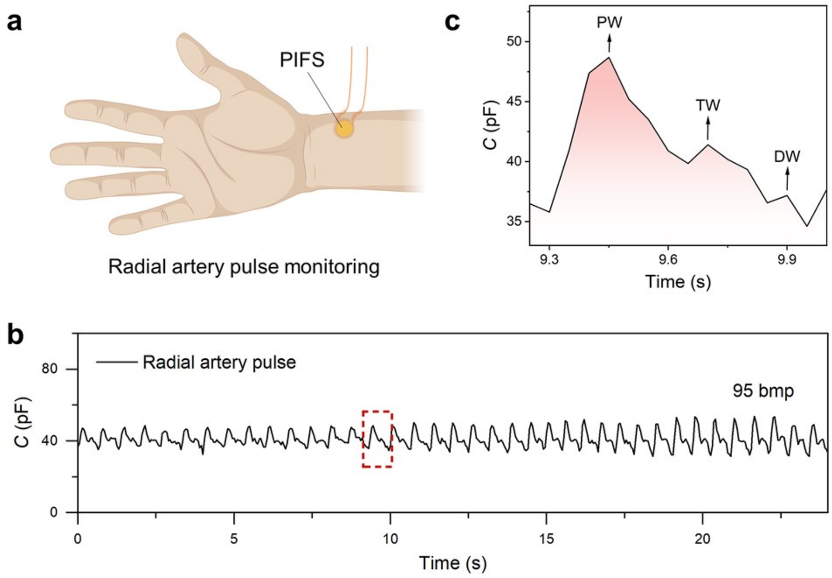

Figure S26. Application of PIFS in wearable devices: (a) Schematic illustration for monitoring the human radial artery pulse. (b) Regular capacitive signal during continuous monitoring of the human radial artery pulse (heart rate ~95 beats per minute). (c) Waveform of a single radial artery pulse (within the red dashed box in (b)). Three characteristic waves can be distinguished: the percussion-wave (PW), tidal-wave (TW), and diastolic-wave (DW).

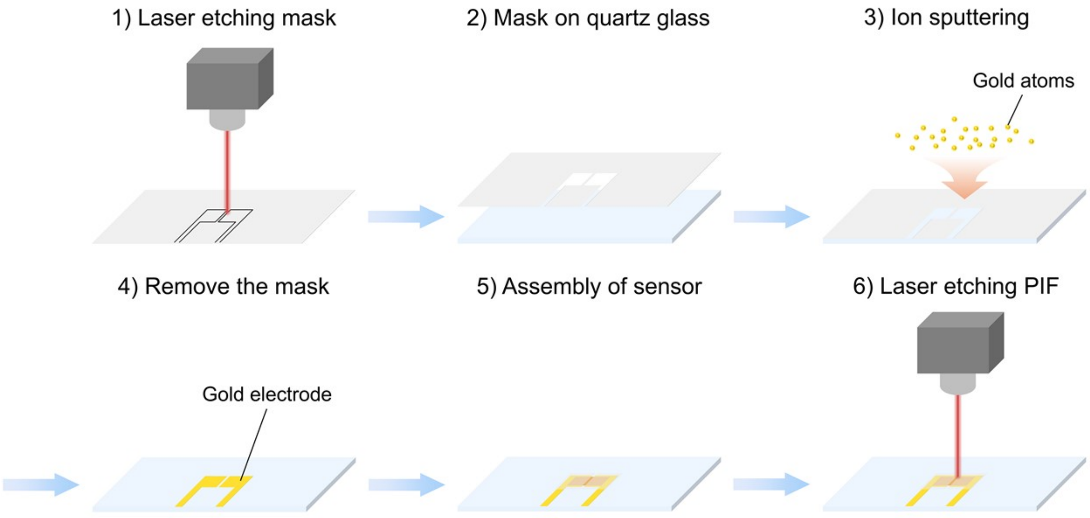

Figure S27. Schematic illustration of the fabrication process for PIF-based iontronic micro-strain sensor.

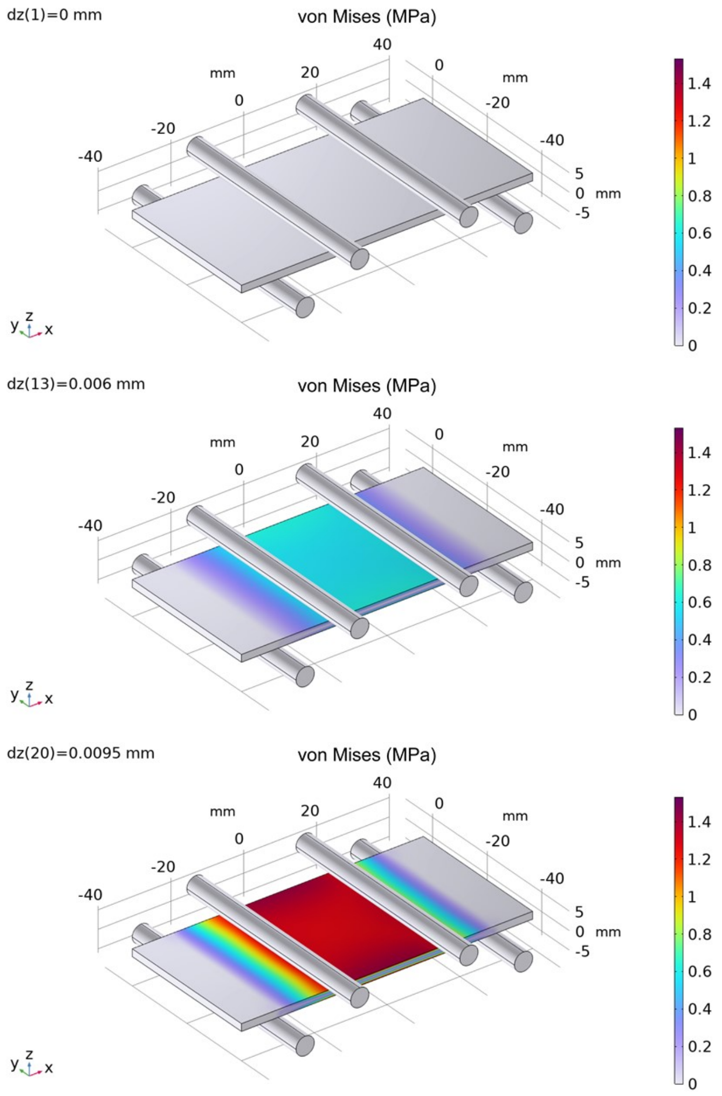

Figure S28. Stress distribution in quartz glass during 3D-FEA of the four-point bending model, with tensile strains at the center of the lower surface of 0, ~10 ppm, and ~20 ppm, corresponding to steel column compressive displacements of 0, 6 μm, and 9.5 μm.

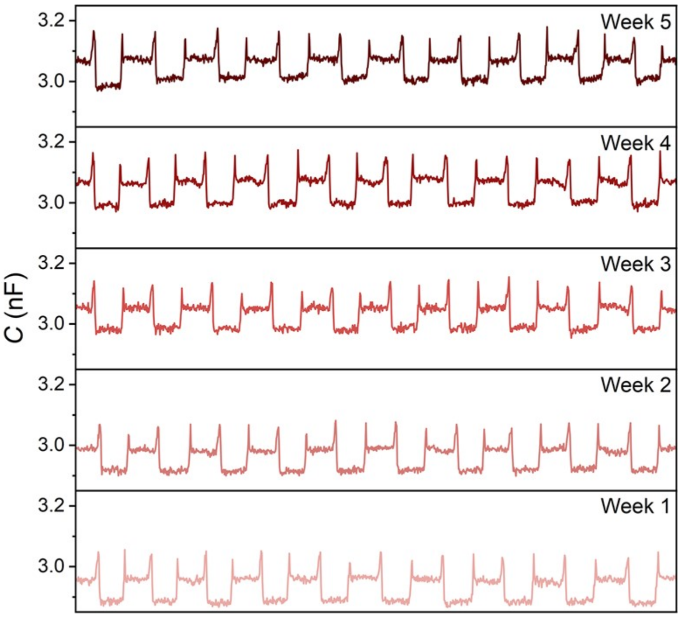

Figure S29. Capacitance change of micro-strain sensor based on the straight slit interconnect structure under 2 N loading pressure over 5 weeks (recorded every 7 days, 10 cycles per recording).

Table S1. Comparison of microparticle dimension characteristics, morphology, and post-film-formation IL retention and ionic conductivity obtained from PAA precursor solutions of different concentrations and viscosities.

PAA concentration (wt%, in DMAc)	Precursor solution viscosity (mPa·s, 20 °C)	Length of microparticles (μm)	Aspect ratio (Fibrous microparticles)	Morphology of microparticles	IL retention (%)	Ionic conductivity (mS/cm)
3	8.3–8.6	27.9 ± 1.5	14.59–23.52	Only irregular and needle-like (<50 μm in length) fragments	83.47 (0 MPa)	6.53 (0 MPa)
					54.44 (5 MPa)	0.887 (5 MPa)
					40.66 (10 MPa)	0.101 (10 MPa)
5	18.4–18.8	89.1 ± 11.9	31.13–69.18	Mostly short fibers (<100 μm), with a small amount of debris	80.92 (0 MPa)	6.13 (0 MPa)
					51.23 (5 MPa)	0.812 (5 MPa)
					41.26 (10 MPa)	0.284 (10 MPa)
10	128–131	225.2 ± 9.4	56.64–103.35	The length of fibers has increased, with a small number of long fibers (>500 μm) and ribbons appearing	79.04 (0 MPa)	4.73 (0 MPa)
					50.83 (5 MPa)	0.747 (5 MPa)
					40.52 (10 MPa)	0.358 (10 MPa)
15	869–877	353.9 ± 18.7	72.71–135.49	The length and diameter of fibers further increase, and the number of ribbons rises	83.10 (0 MPa)	3.37 (0 MPa)
					45.90 (5 MPa)	0.641 (5 MPa)
					37.72 (10 MPa)	0.354 (10 MPa)
20	5906–5968	426.9 ± 12.1	81.33–174.21	Long fibers (>300 μm) dominate, with an increased proportion of ribbons and sheets	82.34 (0 MPa)	2.85 (0 MPa)
					42.63 (5 MPa)	0.540 (5 MPa)
					35.38 (10 MPa)	0.297 (10 MPa)

Table S2. Fitting results of electromechanical properties for iontronic pressure sensors based on various PIFs.

Ionic conductor layer	Pressure range (kPa)	Sensitivity (kPa^{-1})	Linearity
$\mathrm{P_{3}IF_{0}}$	0–5	S_1=0.61	-
	5–15	S_2=1171.07	R_2^2=0.9675
	15–140	S_3=80.40	R_3^2=0.9690
	140–500	S_4=29.40	R_4^2=0.9825
$\mathrm{P_{3}IF_{5}}$	0–10	S_1=2.18	-
	10–100	S_2=78.47	R_2^2=0.9837
	100–500	S_3=30.36	R_3^2=0.9868
$\mathrm{P_{3}IF_{10}}$	0–500	S=5.84	R^2=0.9986
$\mathrm{P_{5}IF_{0}}$	0–10	S_1=18.83	R_1^2=0.9284
	10–50	S_2=211.37	R_2^2=0.9764
	50–150	S_3=78.52	R_3^2=0.9773
	150–500	S_4=30.47	R_4^2=0.9902
$\mathrm{P_{5}IF_{5}}$	0–500	S=30.10	R^2=0.9975
$\mathrm{P_{5}IF_{10}}$	0–50	S_1=21.88	R_1^2=0.9126
	50–500	S_2=9.21	R_2^2=0.9995
$\mathrm{P_{10}IF_{0}}$	0–10	S_1=22.67	-
	10–200	S_2=71.94	R_2^2=0.9654
	200–500	S_3=25.01	R_3^2=0.9561
$\mathrm{P_{10}IF_{5}}$	0–12	S_1=1.15	R_1^2=0.8207
	12–500	S_2=30.61	R_2^2=0.9985
$\mathrm{P_{10}IF_{10}}$	0–15	S_1=2.03	R_1^2=0.9156
	15–500	S_2=9.15	R_2^2=0.9957
$\mathrm{P_{15}IF_{0}}$	0–10	S_1=13.22	R_1^2=0.9582
	10–200	S_2=242.13	R_2^2=0.9371
	200–500	S_3=32.01	R_3^2=0.9734
$\mathrm{P_{15}IF_{5}}$	0–50	S_1=6.08	R_1^2=0.9327
	50–500	S_2=26.43	R_2^2=0.9966
$\mathrm{P_{15}IF_{10}}$	0–500	S=9.11	R^2=0.9819
$\mathrm{P_{20}IF_{0}}$	0–10	S_1=0.88	R_1^2=0.7814
	10–100	S_2=123.83	R_2^2=0.9676
	100–500	S_3=22.05	R_3^2=0.9634
$\mathrm{P_{20}IF_{5}}$	0–500	S=16.60	R^2=0.9966
$\mathrm{P_{20}IF_{10}}$	0–25	S_1=18.26	R_1^2=0.9833
	25–500	S_2=5.80	R_2^2=0.9935

Table S3. Comparison of sensing performance in representative work.

Ionic conductor layer	**Working range (kPa)**	**Sensitivity (kPa^{-1})**	**Linearity**	**Response/Recovery time (ms)**	**Cycling stability (times)**	**Ref.**
P$_3$IF$_0$	0–5 5–15 15–140 140–500	S_1=0.61 S_2=1171.07 S_3=80.40 S_4=29.40	/ R_2^2=0.9675 R_3^2=0.9690 R_4^2=0.9825	/	/	This work (untreated)
P$_3$IF$_5$	0–10 10–100 100–500	S_1=2.18 S_2=78.47 S_3=30.36	/ R_2^2=0.9837 R_3^2=0.9868	10/24	5000	This work (cold-pressed)
TSPU+IL	0–2 2–30 30–300	S_1=1.42 S_2=12.29 S_3=16.77	/ / R_3^2=0.9997	18/21	150000	[5]
PAAm/NaCl hydrogel	0.035–70 70–150 150–330	S_1=0.24 S_2=1.5 S_3=0.13	/	18/36	1500	[6]
PVDF+IL	0–0.5 0.5–120	S_1=1.194 S_2=0.109	/	40/78	5000	[7]
MXene+PVA +LiTFSI	0–30 30–250	S_1=5.5 S_2=1.5	R_1^2=0.997 /	70.4/92.8	20000	[8]
PVA+H$_3$PO$_4$	0–2 2–20	S_1=0.651 S_2=0.016	/	50/80	1200	[9]
TPU+IL	0–100	S =3.997	R^2=0.999	120/60	5000	[10]
P(VDF-HFP) +IL (cross-linked)	0–1 1–10	S_1=4.5 S_2=2	R^2=0.98	50/50	500	[11]
P(AMT-*co*-MA)	0–200 200–500	S_1=3.3 S_2=2.6	/	3.8/5.8	1000	[12]
Human skin	0–3 3–4 4–15	S_1=1.3 S_2=11.8 S_3=2.8	/	15/15	5000	[13]
P(VDF-HFP) +IL (blended)	0-1700	S =33.7	R^2=0.996	6/11	4500	[14]
PDMS-ionogel +P(VDF-HFP)	0-1.5 1.5-10	S_1=0.43 S_2=0.1	/	/	/	[15]
CSN ionogel	0-12 12-20	S_1=15.1 S_2=5.7	/	20/40	1000	[16]
PAN+IL	0-50 50-300	S_1=4.76 S_2=3.1	R_1^2=0.992 R_2^2=0.998	126/131	2000	[17]

References

1. R. S. Bang, S. Roh, A. H. Williams, S. D. Stoyanov and O. D. Velev, *Adv. Mater.*, 2023, **35**, 2211438.
2. S. Roh, A. H. Williams, R. S. Bang, S. D. Stoyanov and O. D. Velev, *Nat. Mater.*, 2019, **18**, 1315–1320.
3. Z. Zhai and T. M. Koller, *Int. J. Thermophys.*, 2023, **44**, 118.
4. Q. Li, M. Cheng, K. Tian, C. Chen, M. Wen and H. Deng, *Adv. Funct. Mater.*, 2026, e32179.
5. B. Zhu, J. Guo, W. Li, T. Luo, F. Lei, G. Li and J. Yang, *Adv. Funct. Mater.*, 2024, **34**, 2406762.
6. Z. Shen, X. Zhu, C. Majidi and G. Gu, *Adv. Mater.*, 2021, **33**, 2102069.
7. Q. Liu, Z. Liu, C. Li, K. Xie, P. Zhu, B. Shao, J. Zhang, J. Yang, J. Zhang, Q. Wang and C. F. Guo, *Adv. Sci.*, 2020, **7**, 2000348.
8. S. Sharma, A. Chhetry, S. Zhang, H. Yoon, C. Park, H. Kim, M. Sharifuzzaman, X. Hui and J. Y. Park, *ACS Nano*, 2021, **15**, 4380–4393.
9. B. Shao, S. Zhang, Y. Hu, Z. Zheng, H. Zhu, L. Wang, L. Zhao, F. Xu, L. Wang, M. Li and J. Shi, *Nano Lett.*, 2024, **24**, 4741–4748.
10. X. Wang, G. Wu, X. Zhang, F. Lv, Z. Yang, X. Nan, Z. Zhang, C. Xue, H. Cheng and L. Gao, *Adv. Mater.*, 2025, **37**, 2410312.
11. Q. Su, Q. Zou, Y. Li, Y. Chen, S.-Y. Teng, J. T. Kelleher, R. Nith, P. Cheng, N. Li, W. Liu, S. Dai, Y. Liu, A. Mazursky, J. Xu, L. Jin, P. Lopes and S. Wang, *Sci. Adv.*, 2021, **7**, eabi4563.
12. Y. He, Y. Cheng, C. Yang and C. F. Guo, *Nat. Mater.*, 2024, **23**, 1107–1114.
13. P. Zhu, H. Du, X. Hou, P. Lu, L. Wang, J. Huang, N. Bai, Z. Wu, N. X. Fang and C. F. Guo, *Nat. Commun.*, 2021, **12**, 4731.
14. R. Yang, A. Dutta, B. Li, N. Tiwari, W. Zhang, Z. Niu, Y. Gao, D. Erdely, X. Xin, T. Li and H. Cheng, *Nat. Commun.*, 2023, **14**, 2907.
15. M.-F. Lin, J. Xiong, J. Wang, K. Parida and P. S. Lee, *Nano Energy*, 2018, **44**, 248–255.
16. X. He, B. Zhang, Q. Liu, H. Chen, J. Cheng, B. Jian, H. Yin, H. Li, K. Duan, J. Zhang and Q. Ge, *Nat. Commun.*, 2024, **15**, 6431.
17. S. Wang, X. Yan, T. Zhang, L. Li, R. Li, S. Ramakrishna, Y.-Z. Long and W. Han, *Adv. Mater. Technol.*, 2024, **9**, 2301791.